

# Linear Approach to Axial Resolution in Elasticity Imaging

Jie Liu, Craig K. Abbey, and Michael F. Insana, *Member, IEEE*

**Abstract**—Thus far axial resolution in elasticity imaging has been addressed only empirically. No clear analytical approaches have emerged because the estimator is nonlinear in the data, correlation functions are nonstationary, and system responses vary spatially. This paper describes a linear systems approach based on a small-strain impulse approximation that results in the derivation of a local impulse response (LIR) and local modulation transfer function (LMTF). Closed-form solutions for strain LIR are available to provide new insights on the role of instrumentation and processing on axial strain resolution. Novel phantom measurements are generated to validate results. We found that the correlation window determines axial resolution in most practical situations, but that the the same system properties that determine B-mode resolution ultimately limit elasticity imaging.

## I. INTRODUCTION

MANY imaging devices are conveniently modeled as linear systems despite the fact that few, if any, are truly linear. Nonetheless, linear approximations lead to accurate predictions of engineering features that summarize important aspects of image quality within the limitations of the assumptions. This paper describes a linear system approach to elasticity imaging that predicts axial resolution.

The diagnostic utility of elasticity imaging depends in part on its ability to spatially resolve objects with distinct viscoelastic properties. For example, malignant epithelial cells in breast cancer send molecular signals to stromal cells that upregulate collagen production and increase crosslinking to stiffen cells in the region [1]. Elasticity can help to identify these malignancies if the margins of the lesion in the strain image can be delineated accurately for comparison with the corresponding B-mode image [2]. Also, vascular elasticity imaging requires sub-millimeter resolution to distinguish media and adventitia layers [3]. Intuition suggests that the upper limit for the axial resolution of displacement and strain estimates is determined by properties of the ultrasonic system acquiring the data. Therefore, carrier frequency, bandwidth, and aperture of the transducer are key elements. However, the correlation window dimensions, differentiation and interpolation filters, nonlinear estimators, and regularization methods applied to reduce noise also must affect resolution. If the procedure includes static deformation, then

the object shape and the applied mechanical stimulus are additional factors.

Spatial resolution of strain images has been measured using phantoms with spherical and cylindrical targets in uniform backgrounds. Echo data were simulated [4], [5] or recorded from gelatin phantoms [6], and the Rayleigh criterion was applied to assess axial and lateral resolution; the latter study made connections to the modulation transfer function (MTF) computed from echo simulations. They found that strain resolution is indeed ultimately limited by transducer properties as intuition suggests. However, no one has yet analyzed this important problem analytically to show how contributing elements interact to determine the measured axial resolution. The methods presented in this report make it possible to determine situations in which axial strain resolution is being limited by the strain estimator (in which case a better estimator is needed) or is more fundamentally limited by the transducer properties. The ability to isolate limiting sources is very difficult to do by empirical methods.

This paper gives a general statement of the strain imaging problem, describes a one-dimensional (1-D) analytical method for computing the local impulse response (LIR) and associated local MTF (LMTF), and verifies predictions using simulation and phantom measurements. The phantom is designed to approximate a 1-D strain impulse that enables us to isolate sources of blur caused by instrumentation and processing that are independent of object features.

## II. ACQUISITION AND ESTIMATION: THE GENERAL PROBLEM

The object function  $f_j(\mathbf{x})$  describes the distribution of scattering sources during acquisition of the  $j$ th echo frame. It is a function of continuous vector position  $\mathbf{x}$ , and it can be deterministic, a realization of a stochastic process, or contain elements of both. Relative scatterer motion is observed by examining an object during two or more instances in time; e.g., at frame  $j$  and  $j+1$ . These are related by a displacement vector  $\mathbf{d}_{j+1}(\mathbf{x})$  that describes the movement of scatterers between times that the two frames are recorded:

$$\begin{aligned} f_{j+1}(\mathbf{x}) &= f_j(\mathbf{x} + \mathbf{d}_{j+1}(\mathbf{x})) \\ &= \int_{-\infty}^{\infty} dx' f_j(\mathbf{x}') \delta(\mathbf{x}' - \mathbf{x} - \mathbf{d}_{j+1}(\mathbf{x})), \end{aligned} \quad (1)$$

where  $\delta(\mathbf{x})$  is the multidimensional Dirac delta (integral one). The linear shift-variant form of (1) requires the object  $f$  to be functionally independent of displacement  $\mathbf{d}$ ,

Manuscript received September 8, 2003; accepted January 15, 2004. This work was supported in part by NIH R01 CA82497 and Siemens Medical Solutions, Inc. USA, Ultrasound Division.

The authors are with the Department of Biomedical Engineering, University of California-Davis, Davis, CA (e-mail: jliu@ucdavis.edu).

which is often valid for small deformations. Movement of scatterers out of the imaging plane is one situation in which the assumption fails.

To describe strain estimators operating on discretely sampled data, it is convenient to adopt a matrix form. Imagine sampling a continuous object on an interval small compared to that of echo sampling to yield an  $N_f \times 1$  object vector  $\mathbf{f}_j$  in  $\mathbb{R}^3$ . Samples from a 3-D object can be arranged into the 1-D column vector by lexicographical reordering [7]. Consequently, (1) can be rewritten as:

$$\mathbf{f}_{j+1} = \mathbf{Q}_{j+1}\mathbf{f}_j + \mathbf{e}_{j+1}^r, \quad (2)$$

where  $\mathbf{e}_{j+1}^r$  represents registration errors arising from sampling. Shifts in scatterer position represented by an integral transformation in (1) are now expressed by a matrix multiplication in (2).  $\mathbf{Q}_{j+1}$ , a square  $N_f \times N_f$  operator matrix, describes the spatial transformation of scatterer positions that occurs between frames  $j$  and  $j+1$ .

Scanning the object with a linear imaging system, we acquire the following pre- and postdeformation echo data vectors:

$$\begin{aligned} \mathbf{g}_j &= \mathbf{H}\mathbf{f}_j + \mathbf{e}_j, \\ \mathbf{g}_{j+1} &= \mathbf{H}\mathbf{Q}_{j+1}\mathbf{f}_j + \mathbf{e}_{j+1}, \end{aligned} \quad (3)$$

where the noise vectors  $\mathbf{e} = \mathbf{H}\mathbf{e}^r + \mathbf{e}^a$  include both registration errors and acquisition noise.  $\mathbf{H}$  is an  $N_g \times N_f$  system matrix whose rows are the impulse response at each spatial location. It maps the  $N_f \times 1$  object vector  $\mathbf{f}$  into a lower dimensional  $N_g \times 1$  data vector  $\mathbf{g}$ , describes the coherent summation of scattered waves at the aperture, and thus the effects of downsampling, speckle and blur. This summarizes the forward problem.

In the inverse problem, displacements can be found by analyzing echo signals if the deformation of the object described in (3) can be approximated by a deformation of the echo signal:

$$\mathbf{g}_{j+1} \simeq \mathbf{D}_{j+1}\mathbf{H}\mathbf{f}_j + \mathbf{e}_{j+1}.$$

In those situations, displacements may be estimated from pairs of echo frames using constrained optimization; specifically, we seek  $\mathbf{D}'$  that minimizes the objective function [7]:

$$\hat{\mathbf{D}}_{j+1} = \arg \min_{\mathbf{D}'} (\|\mathbf{g}_{j+1} - \mathbf{D}'\mathbf{g}_j\|^2 + \alpha\|\mathbf{r}\|^2). \quad (4)$$

$\|\cdot\|$  is the vector norm, and  $\mathbf{r}$  is a roughness penalty vector [8] and a function of the displacement vector  $\mathbf{d}'(\mathbf{x})$  [9], [10].  $\alpha$  is a constant that controls the trade-off between fidelity of estimates to the data via  $\|\mathbf{g}_{j+1} - \mathbf{D}'\mathbf{g}_j\|^2$  and the smoothness of the solution via  $\|\mathbf{r}\|^2$ . In situations in which  $\mathbf{g}_j$  and  $\mathbf{g}_{j+1}$  are highly correlated, we set  $\alpha \simeq 0$  to accurately estimate the displacement vectors, i.e.,  $\hat{\mathbf{D}} \simeq \mathbf{D}$ . However, in regions in which the echo correlation coefficient deviates significantly from 1, decorrelation noise is reduced at the cost of biasing estimates by increasing  $\alpha$ . Note that the minimum value of the objective function in (4) is  $\|\mathbf{e}_{j+1} - \mathbf{D}_{j+1}\mathbf{e}_j\|^2$  at  $\mathbf{D}' = \mathbf{D}_{j+1}$ ,  $\alpha = 0$ , so that noise minimization is essential.

Implementation of (4) has been studied for strain estimation using a variety of algorithms [8]–[13]. However, by far, the simplest and most widely used approach to solving (4) is cross correlation; and (4) is equivalent to maximization of the cross-correlation function when  $\alpha = 0$  and the signal energy does not change significantly during deformation, e.g.,  $\|\mathbf{D}'\mathbf{g}_j\|^2 \simeq \|\mathbf{g}_{j+1}\|^2$ . Consequently, for relatively small deformations [13], the maximum likelihood estimator for displacement is:

$$\hat{\mathbf{D}} = \arg \max_{\mathbf{D}'} (\mathbf{g}_{j+1}, \mathbf{D}'\mathbf{g}_j), \quad (5)$$

where  $(\mathbf{g}_{j+1}, \mathbf{D}'\mathbf{g}_j)$  is the inner product of the vectors. Displacement estimators in (4) and (5) are nonlinear in the data. Strain tensors are found from linear combinations of spatial derivatives of displacement taken along the coordinate axes [14].

Eq. (3)–(5) are statements of the general ultrasonic strain estimation problem, independent of estimation technique, in which local displacements resulting from an applied stress stimulus are estimated by comparing echoes recorded at different times.

Eq. (5) shows that the cross-correlation function is an essential feature of displacement measurements in deformed random scattering media. The presence of echo noise requires spatial averaging of correlation function estimates to reduce displacement errors. Yet only rigid transformations (i.e., zero-strain conditions and linear shift-invariant imaging systems) yield position independent (stationary) correlation. Consequently, applying any strain at all to the object produces nonstationary correlation function.

We are proposing a linear, Fourier-based analysis of spatial resolution for strain imaging that accurately predicts measurements, over a reasonable range of global deformation (<5%), despite the nonstationarity of the correlation estimates for nonzero strain, the nonlinearity of the estimator, and the use of shift-variant imaging systems. The approach is to analyze the response of the system to a small-amplitude, strain impulse. The resulting correlation function is piecewise stationary, except in the small interval in which the strain is nonzero. Images of a strain impulse yield measurements of LIR [15] whose Fourier transform gives the LMTF of the system. We derive expressions for displacement and strain, then test them using simulated echo data and phantom measurements.

### III. CORRELATION FOR A 1-D STRAIN IMPULSE

To simplify the analysis, echo samples  $g_j[n]$  from frame  $j$  are modeled as arising from a 1-D object function  $f_j(x)$  through the continuous-to-discrete integral transformation [16]:

$$g_j[n] = \int_{-\infty}^{\infty} dx h(nT, x) f_j(x) + e_j[n]. \quad (6)$$

Parentheses and brackets indicate functions of continuous and discrete variables, respectively.  $h(t, x)$  maps spatially varying object functions into time-varying data vectors that are sampled on the time interval  $T$ , such that  $t = nT$  for integer  $n$ .  $e[n]$  are samples of a signal independent noise vector. It is assumed that  $f$  and  $e$  are drawn from wide-sense stationary (WSS) random processes, and that  $f_1(x) = f(x)$  and  $f_2(x) = f(x + d(x))$ . Instead of solving for the entire displacement field simultaneously, as suggested by (5), we segment echo vectors with overlapping window functions and compute the average displacement at each windowed location.

To study axial resolution, we apply a strain “impulse” at location  $x_s$ . More precisely, it is a rectangular function of magnitude  $s/X_s$  and length  $X_s$ , i.e.,  $\epsilon(x) = (s/X_s) \cdot \text{rect}((x - x_s)/X_s)$ . It may be considered an impulse when the sampling interval equals the length  $X_s = cT/2$ , where  $c$  is the longitudinal sound speed. We impose the physical constraint that the displacement is less than the interval  $|s| \leq cT/2$  to prevent “folding” that occurs when  $\epsilon > 1$ . The corresponding displacement profile is a ramp function:

$$d(x) = \int_{-\infty}^{\infty} \epsilon(x') dx' = \frac{s}{X_s} \int_{-\infty}^x \text{rect}\left(\frac{x' - x_s}{X_s}\right) dx'$$

$$\begin{cases} 0 & x < x_s - X_s/2 \\ \frac{(x - x_s + X_s/2)s}{X_s} & x_s - X_s/2 \leq x \leq x_s + X_s/2 \\ s & x > x_s + X_s/2 \end{cases} \quad (7)$$

In the continuous limit,  $X_s \rightarrow 0$  and  $d(x) = s \int_{-\infty}^x \delta(x' - x_s) dx' = s \cdot \text{step}(x - x_s)$ , i.e., the ramp becomes a step function and the strain profile is a true impulse; (7) is approximated experimentally by compressing a phantom consisting of a thin, soft layer surrounded by stiff, thick layers as described in Section VI. Note that, for a compressive stimulus,  $\epsilon$ ,  $d$ , and  $s$  have negative values.

Displacement is estimated by windowing and cross correlating  $g_j$  with  $g_{j+1}$ , interpolating the result, and locating the peak. Estimates  $\hat{d}(x)$  correspond to the lag at the correlation peak. The axial strain profile  $\hat{\epsilon}(x)$  is given by the spatial derivative of  $\hat{d}(x)$ . Let us examine the details of this estimator for an ideal imaging system.

#### A. Ideal System

Eq. (6) for an ideal imaging system  $h(t) = \delta(t)$  without noise gives the echo signal  $g_j[n] = f(ncT/2) = f[n]$ .  $g_j$  and  $g_{j+1}$  are multiplied by the same rectangular window function  $w[n] = \text{rect}((n - n_m)/N)$  to give  $g'_j$  and  $g'_{j+1}$ , where  $N = 2(x_2 - x_1)/cT + 1$  is the number of samples in the data window,  $n_m = (x_1 + x_2)/cT$  identifies the center sample in the window, and  $n_1 = 2x_1/cT$ ,  $n_2 = 2x_2/cT$ . Windowed echo signals from the ideal system are sampled object functions plus noise (Fig. 1):

$$g'_j[n] = \begin{cases} f[n] + e_j[n] & n_1 \leq n \leq n_2 \\ 0 & \text{otherwise} \end{cases}, \quad (8a)$$

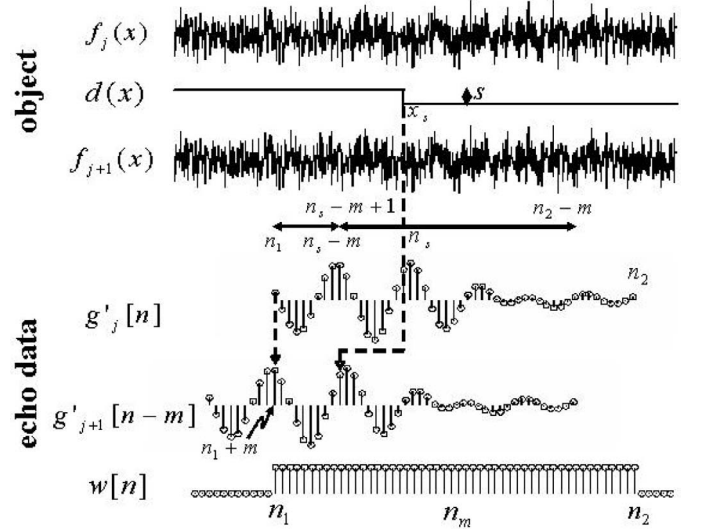


Fig. 1. Signals before and after an impulse deformation. An object  $f_1(x)$  undergoes a step displacement  $d(x) = s \text{step}(x - x_s)$  to give  $f_2(x)$ . Echo waveforms are generated before and after deformation, sampled, and range gated using  $w[n]$  to give the digital echo samples  $g'_1[n]$  and  $g'_2[n]$ . Displacements are estimated by analyzing cross-correlation estimates at lag  $m$ .

$$g'_{j+1}[n] = \begin{cases} f[n] + e_{j+1}[n] & n_1 \leq n \leq n_s \\ f_s[n] + e_{j+1}[n] & n_s + 1 \leq n \leq n_2 \\ 0 & \text{otherwise} \end{cases} \quad (8b)$$

The function  $f_s$  includes shifts in the continuous object function that can be smaller than the sampling interval of the data. An arbitrary shift may be applied with minimal artifact to a discretely sampled signal by bandlimited sinc interpolation of  $f[n]$ , shifting, and resampling [17]. The result is a convolution:

$$f_s[n] = \sum_{n'=-\infty}^{\infty} f[n'] \frac{\sin \pi(n - n' - 2s/cT)}{\pi(n - n' - 2s/cT)} = (h_s * f)[n], \quad (9)$$

where the interpolation filter is  $h_s[n] = \text{sinc}(n - 2s/cT)$ . For the special case  $\epsilon(x) = -\text{rect}(2(x - x_s)/cT)$ , there is a shift of one sampling interval  $s = -cT/2$  at position  $x_s$  so that  $h_s[n] = \delta[n + 1]$  and  $f_s[n] = f[n + 1]$ .

A biased estimate of the cross-correlation function for one signal pair  $\hat{\phi}_{g'_j g'_{j+1}}$  is often time averaged over the window function  $w$  to give [18]:

$$\begin{aligned} \bar{\phi}_{g'_j g'_{j+1}}[n_m, n_m - m] &= \frac{1}{N} \sum_{n=n_1}^{n_2-m} g'_j[n] g'_{j+1}[n - m] \\ &= \frac{1}{N} \left[ \sum_{n=n_1}^{n_s-m} f[n] f[n - m] + \text{Noise} \right. \\ &\quad \left. + \sum_{n=n_s-m+1}^{n_2-m} f[n] f_s[n - m] \right]; \quad 0 \leq m \leq N. \end{aligned} \quad (10)$$

Noise-noise and noise-signal terms are lumped into one term labeled noise. Time averaging is applied to reduce variability generated by the random object function and noise. This is allowed because  $f_{j+1}$  is piecewise WSS over the segments  $[n_1, n_s]$  and  $[n_s + 1, n_2]$ . Ensemble averaging the time-averaged cross-correlation function for uncorrelated noise gives:

$$\begin{aligned} \overline{\phi}_{g'_j g'_{j+1}}[n_m, n_m - m] &= \varepsilon \left\{ \overline{\phi}_{g'_j g'_{j+1}} \right\} = \overline{\phi}_{f'_j f'_{j+1}} \\ &= \frac{1}{N} \left[ \sum_{n=n_1}^{n_s-m} \phi_{ff}[m] + \sum_{n=n_s-m+1}^{n_2-m} \phi_{fs}[m] \right] \\ &= w_1[n_m, m] \phi_{ff}[m] + w_2[n_m, m] (h_s * \phi_{ff})[m], \end{aligned} \quad (11)$$

where  $\varepsilon\{\cdot\}$  is the expectation operator,  $\phi_{ff}[-m] = \phi_{ff}[m]$ , and  $\phi_{fs}[m] = \varepsilon\{f[n]f_s[n-m]\} = \varepsilon\{f[n+m](h_s * f)[n]\} = (h_s * \phi_{ff})[m]$  for real, WSS  $f$ . Also,  $w_1$  and  $w_2$  weight the correlation sequences depending on window location:

$$\begin{aligned} w_1[n_m, m] &= \begin{cases} (N_1 - m)/N & 0 < m \leq N_1 \\ N_1/N & m \leq 0 \end{cases}, \\ w_2[n_m, m] &= \begin{cases} N_2/N & m \geq 0 \\ (N_2 - |m|)/N & -N_2 \leq m < 0 \end{cases}, \end{aligned} \quad (12)$$

where  $N_1 = n_s - n_1 + 1$  and  $N_2 = n_2 - n_s$ . We only considered positive correlation lags in (10) and (11). The sum limits change to  $\sum_{n_1-m}^{n_s-m} + \sum_{n_s-m+1}^{n_2}$  when  $m < 0$ , as with compression, and so the weighting windows depend on the sign of  $m$  as shown in (12). Without deformation, (11) becomes  $\overline{\phi}_{g'_j g'_2}[m] = ((N - |m|)/N) \phi_{ff}[m] \forall m$ .

Given the step displacement profile of (7), we find that:

$$\begin{aligned} \phi_{ff}[m] &= a^2 \delta[m], \\ \phi_{fs}[m] &= a^2 \text{sinc}(m - 2s/cT), \end{aligned} \quad (13)$$

where  $a^2 \triangleq \varepsilon\{|f[n]|^2\}$  and  $\delta[m]$  is the Kronecker delta of amplitude one at  $m = 0$  and zero otherwise. A sub-sample shift in the uncorrelated random object function yields a sinc correlation function with zeros positioned at  $x = k(1 + 2s/cT)$  for  $k = \pm 1, \pm 2, \dots$ . Sinc interpolation is exact for signals of infinite length. However, a more practical expression for  $\phi_{fs}$  is obtained by applying the linear interpolation filter [17]:

$$\phi_{fs}[m] \simeq \begin{cases} a^2 |1 - |m| - 2|s|/cT| & |m| \leq 1 \\ 0 & \text{otherwise} \end{cases}. \quad (14)$$

Recall that  $n_m = (n_2 + n_1)/2$  identifies the echo sample at the center of the time window. Combining (11)–(14)

we find the cross-correlation function for a compressive step displacement is:

$$\begin{aligned} \overline{\phi}_{g'_j g'_{j+1}}[n_m, n_m - m] &= a^2 \delta[m]; \quad n_m - n_s < -N/2 \\ &= \begin{cases} \frac{a^2}{N} (N_1 + N_2(1 - 2|s|/cT)) & m = 0 \\ (2a^2|s|/cT)(N_s/N) & m = 1; |n_m - n_s| < N/2 \\ 0 & \text{else} \end{cases} \\ &= \begin{cases} a^2(1 - 2|s|/cT) & m = 0 \\ 2a^2|s|/cT & m = 1; \quad n_m - n_s > N/2 \\ 0 & \text{else} \end{cases} \end{aligned} \quad (15)$$

where  $N_1 = -n_m + n_s + \frac{N+1}{2}$  and  $N_2 = n_m - n_s + \frac{N-1}{2}$ . Referring to Fig. 1, the three regions in  $n_m$  define the correlation function when the window is to the left of the strain impulse, includes the strain impulse, and is to the right of the strain impulse.

The exact location of the correlation peak in each region can be found by applying a second-order Lagrange (quadratic) interpolator to  $\overline{\phi}_{g'_1 g'_2}$  about the lag sample nearest the peak. We define  $\epsilon_a \triangleq |2s/cT|$  as the magnitude of the strain impulse at  $x_s$ . When  $-1 < \epsilon_a < -0.5$ , the peak will occur at  $m = 1$ . However when  $-0.5 \leq \epsilon_a \leq 0$ , which we assume in what follows, the peak will occur at  $m = 0$ . Interpolating the correlation function about the origin, differentiating and setting the result equal to zero, we find the following nonlinear estimator:

$$\hat{d}[n_m] = \frac{cT(\overline{\phi}_{g'}[n_m, -1] - \overline{\phi}_{g'}[n_m, 1])}{4(\overline{\phi}_{g'}[n_m, -1] - 2\overline{\phi}_{g'}[n_m, 0] + \overline{\phi}_{g'}[n_m, 1])}. \quad (16)$$

Here we abbreviated  $\overline{\phi}_{g'_j g'_{j+1}}[n_m, n_m - m]$  as  $\overline{\phi}_{g'}[n_m, m]$ ; (16) is analogous to (5) for the strain impulse experiment. Displacement is measured over the axial range  $1 \leq n_m \leq M$ .

To illustrate, let us apply a 50% compressive strain over one sampling interval located at  $x_s$ , i.e.,  $\epsilon(x) = -0.5 \cdot \text{rect}(2(x - x_s)/cT)$ . In the first region of (15), in which the correlation window is entirely to the left of the strain impulse (Fig. 1), the correlation function is simply  $a^2 \delta[m]$ , and from (16) we find the estimate  $\hat{d}[n_m] = 0$ . In the third region of (15), in which the correlation window is entirely to the right of the strain impulse, the two nonzero values of the correlation function both equal  $a^2/2$ , and indeed (16) yields  $\hat{d}[n_m] = -cT/4$ . However, in the second region of (15), the window straddles the strain impulse and, therefore, estimates are weighted by  $N_1$  and  $N_2$  so that (16) yields:

$$\hat{d}[n_m] = -\frac{cT/4}{4N_1/N_2 + 1}.$$

It is easy to see that at either extreme, where  $N_1/N_2 = N$  or  $1/N$ , the results approach 0 and  $-cT/4$ , respectively, as expected for large  $N$ . More importantly, the effects of the correlation window duration and interpolation function on displacement estimates is available from region two, the only region in which the strain is nonzero.

A general expression for the displacement in the second region of (15) is:

$$\hat{d}_i[n_m] = \frac{cT/4}{3 - 2N/(N_2\epsilon_a)}. \quad (17)$$

### B. Realistic System

The correlation function for a realistic pulse-echo system cannot be expressed as the sum of piecewise WSS processes as in (10). The blur from the finite pulse duration mixes object scatterers located before and after the displacement step. Although this process can be modeled numerically, such results do not provide the physical insights we seek. Instead, we propose simply filtering the displacement estimates of (17) using a digital approximation to the system impulse response  $h[n]$  as in (6). This gives the local impulse response for displacement:

$$\text{LIR}_d[n_m] \triangleq \hat{d}_r[n_m] = \sum_{n=-\infty}^{\infty} h[n_m, n] \hat{d}_i[n]. \quad (18)$$

Imaging systems often have compact impulse response functions, thus shortening the range of summation in (18). The validity of (18) is tested below in applications involving data simulations and phantoms.

## IV. STRAIN LMTF AND AXIAL RESOLUTION

The LIR for strain is estimated from the filtered derivative of (17) with respect to  $n_m$ , or, through a change of variable, with respect to  $N_2$ :

$$\hat{\epsilon}_i[n_m] = -\frac{N}{9\epsilon_a \left(\frac{2N}{3\epsilon_a} - N_2\right)^2} \quad \text{and} \quad (19)$$

$$\text{LIR}_\epsilon[n_m] \triangleq \hat{\epsilon}_r[n_m] = \sum_{n=-\infty}^{\infty} h[n_m, n] \hat{\epsilon}_i[n]. \quad (20)$$

Eq. (20) is finite because the double pole in (19) is outside the range  $1 \leq N_2 \leq N$ ; (19) and (20) express the estimated strain in terms of the applied strain.

The LMTF for strain is the normalized discrete Fourier transform of  $\text{LIR}_\epsilon$  [19]:

$$\text{LMTF}[k] = \frac{|\Xi[k]|}{|\Xi[0]|}, \quad (21)$$

where

$$\Xi[k] \triangleq \mathcal{F}\{\text{LIR}_\epsilon[n_m]\} = \sum_{n_m=0}^{M-1} \hat{\epsilon}_r[n_m] e^{-i2\pi kn_m/M},$$

and  $M$  is the number of strain measurements along each line of site. Output displacement and strain for a strain impulse input and the corresponding LMTF curves are given in Fig. 2. We adopt a common figure of merit for specifying

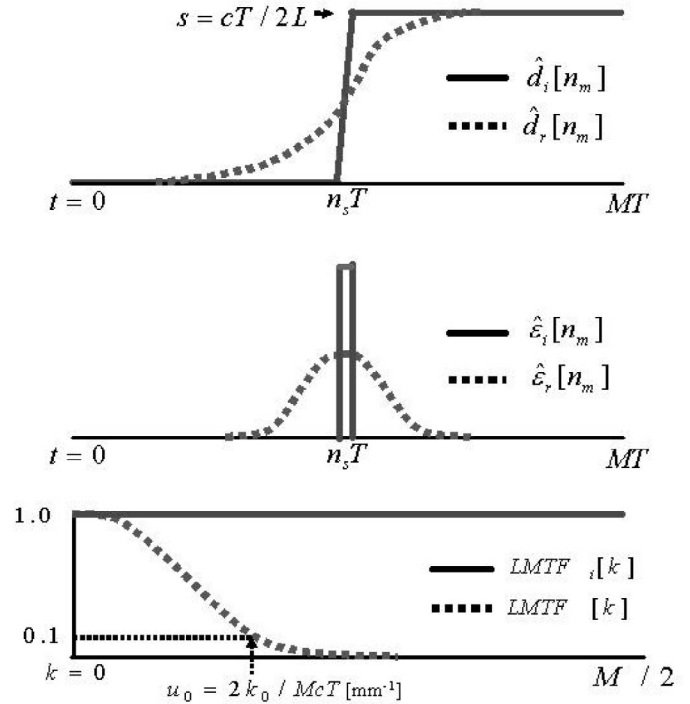


Fig. 2. Displacement profiles estimated for the ideal  $\hat{d}_i$  (17) and realistic  $\hat{d}_r$  (18) imaging systems scanning a strain “impulse” (top). Corresponding  $\text{LIR}_\epsilon$  (19) and (20) (middle), and LMTF (21) (bottom) also are shown.

axial resolution as the inverse value of the lowest spatial frequency  $u_0 = 2k_0/McT$ , at which the LMTF curve drops to 0.1. For example, if  $u_0 = 2 \text{ mm}^{-1}$ , one interpretation is that the system is capable of resolving cyclic strain patterns on a scale larger than two line pairs per millimeter.

The procedure for computing LMTF from experimentally recorded echo data is straightforward.

- Compute  $\hat{\phi}_{g'_1 g'_2}$  for a strain impulse using the the first line of (10).
- Interpolate the result then estimate displacements from the correlation lags at the maximum value of  $\hat{\phi}_{g'}$ , specifically,

$$\hat{d}[n_m] = \frac{cT}{2} \arg \max_m \left( \mathcal{I} \left\{ \hat{\phi}_{g'_j g'_{j+1}} [n_m, n_m - m] \right\} \right)$$

gives  $\text{LIR}_d$  at the location  $n_m$ .  $\mathcal{I}\{\cdot\}$  is the interpolation operator.

- Digitally filter  $\hat{d}[n_m]$  with a finite impulse response (FIR) differentiator  $h_d$  [17] to estimate  $\text{LIR}_\epsilon$ ,

$$\hat{\epsilon}[n_m] = (h_d * \hat{d})[n_m]. \quad (22)$$

- Compute LMTF and  $u_0$  from (21).

The following sections describe echo simulations and phantom experiments that test these ideas.

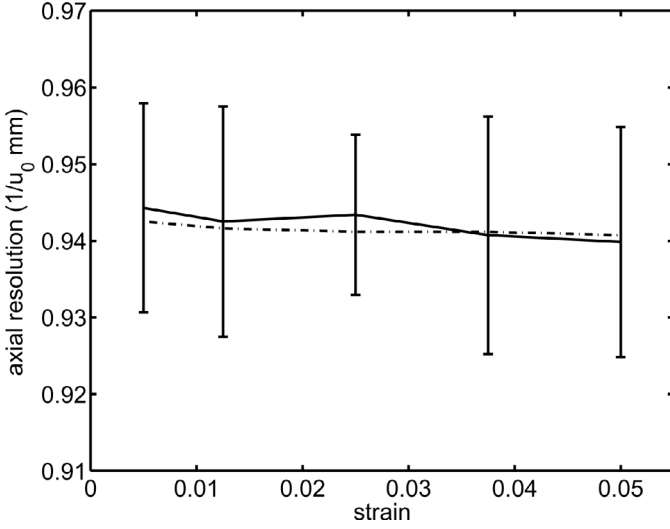


Fig. 3. Using echo simulations, predicted (dash-dotted line) and measured (solid line) values of the axial resolution metric  $1/u_0$  are shown as a function of strain. The pulse-length parameter is  $L_p = 0.35$  mm, and correlation window length is  $NcT/2 = 0.86$  mm. Error bars denote one standard deviation.

## V. ECHO SIMULATIONS AND MEASUREMENTS

Object functions  $f_j$  were generated numerically in 1-D using Monte Carlo methods. The mean number of scatterers positioned along the entire axis was selected to be greater than 20 per pulse length to ensure fully developed speckle conditions. The mean was introduced into a Poisson random number generator to select the actual number of identical point scatterers present for each realization of  $f_j$ .

Next, each scatterer was positioned continuously along the axis using a uniform random number generator on the interval. Consequently, scatterer positions are uncorrelated. A binomial random number generator was used to determine polarity of the scattering amplitude so that the spatial mean value for  $f_j$  was zero.

This object function was convolved with the linear time-invariant impulse response of the system, given by the Gaussian modulated sinusoid  $h(t) = \exp(-t^2/2\sigma_t^2) \sin \omega_0 t$  yield  $g_j$ . The carrier frequency of the pulsed transmission was  $\omega_0/2\pi = 7.2$  MHz,  $c = 1.54$  mm/ $\mu$ s, and  $\sigma_t$  is the pulse-duration parameter (in  $\mu$ s). The pulse-length parameter  $L_p$  (in mm) is related to  $\sigma_t$ , and the effective bandwidth  $B_{\text{eff}}$  (in MHz) using  $L_p = c\sigma_t\sqrt{\pi} = c/(2B_{\text{eff}})$  [13]. We considered pulse lengths in the range of  $0.13\text{mm} \leq L_p \leq 1.63$  mm corresponding to effective fractional bandwidths of  $0.78 \geq B_{\text{eff}}/f_0 \geq 0.065$ . The echo signal then was downsampled, multiplied by a rectangular window function  $w[n]$ , and white Gaussian noise was added (40 dB echo signal-to-noise ratio, SNR) to give the predeformation echo signal  $g'_j[n]$  at a sampling rate of 57.6 Msamples/s.

Given that scatterers were positioned continuously along the axis, they were accurately displaced by applying (7) directly. Deformed object functions  $f_{j+1}$  were sampled, scanned and downsampled via (6), windowed, and noise

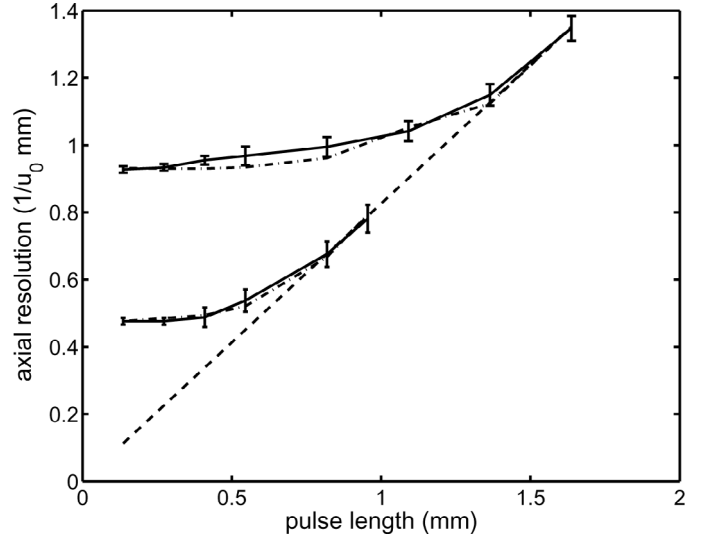


Fig. 4. Using echo simulations, predicted (dash-dotted line) and measured (solid line) values of the axial resolution metric  $1/u_0$  are shown as a function of pulse length. The correlation window length  $NcT/2 = 0.86$  mm (upper curve),  $NcT/2 = 0.43$  mm (lower curve) and applied strain  $\epsilon = 0.05$  were fixed. The dashed line indicates the axial resolution metric for B-mode imaging. Error bars denote one standard deviation.

was added to yield  $g'_{j+1}[n]$ . Deformation before sampling made it unnecessary to apply (9). Strain amplitudes in the typical tissue imaging range  $0.005 \leq \epsilon_a \leq 0.05$  were studied. For each parameter analyzed, sets of 200 independent waveform pairs  $\{g'_j\}$  and  $\{g'_{j+1}\}$  were generated. We computed (10) from each data vector pair and averaged the 200 results to approximate  $\bar{\phi}_{g'_j g'_{j+1}}$ . Subsequently, quadratic interpolation was applied, the lag at the interpolated correlation peak was found, and that result was converted to a displacement to give the  $\text{LIR}_d$ . The LMTF was computed via (21), and  $u_0$  was found to summarize the axial resolution limit of the system.

In Figs. 3–5, axial resolution predictions for different combinations of experimental parameters are compared with measurements obtained from echo simulations. Fig. 3 shows values of  $1/u_0$  for typical measurement conditions. Small values of  $1/u_0$  indicate high-resolution images; in this case, the resolution limit is  $u_0 \simeq 1.06$  lp/mm. Two observations are immediately apparent from Fig. 3. Measurements up to 5% applied strain are accurately predicted by the linear approach, and the axial resolution does not appear to depend on the applied strain.

Fig. 4 shows values of the axial resolution metric  $1/u_0$  for strain imaging and B-mode imaging as a function of the pulse length parameter  $L_p$ , where other parameters are held constant. (Notice that the B-mode resolution with our criterion is proportional but not equal to  $L_p$ .) The B-mode metric does not depend on the correlation window length, of course, but it does decrease with pulse length, suggesting improved axial resolution. We see that the axial resolution for strain imaging is dominated by the window length when it exceeds the pulse length. However, strain resolution is ultimately limited by the pulse length of the

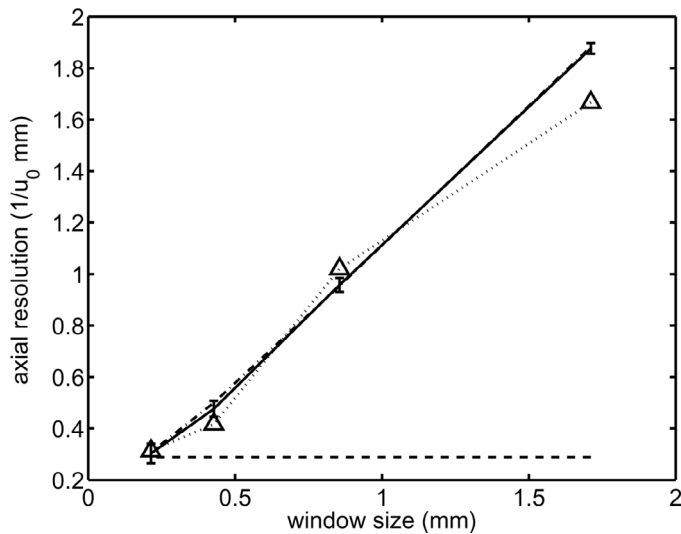


Fig. 5. Comparison of  $1/u_0$  values predicted (dash-dotted line), measured from echo simulations (solid line), and measured from phantom experiments (triangles) as a function of window length. The pulse length  $L_p = 0.35$  mm and applied strain  $\epsilon = 0.05$  were held constant. The dashed line indicates the axial resolution metric for B-mode imaging, and the error bars denote one standard deviation.

ultrasonic system; therefore, B-mode resolution is an accurate estimate of the upper bound for strain resolution.

Fig. 5 shows  $1/u_0$  versus window length when other parameters are held fixed. Again, the pulse length determined the upper bound of strain resolution. The metric increases linearly (strain resolution falls) as the window length exceeds the pulse length, similar to the results found by others [6].

## VI. PHANTOM MEASUREMENTS

Predictions of the analysis and measurements from echo simulation were validated using phantom experiments. The phantom (Fig. 6) has two stiff graphite-in-agar blocks [20] with adjacent planar surfaces oriented normal to the beam axis. Sandwiched between the surfaces was a thin layer of graphite-agar slurry [21]. Once compressed, virtually all strain is concentrated in the soft slurry layer, thus approximating a ramp displacement profile described mathematically by (7). The mean scattering amplitude was approximately constant throughout the field.

Echo data were recorded while scanning the phantom with a Siemens Elegra (Siemens Medical Solutions, Mountain View, CA) system and a 7.5 MHz linear array (7.5L40) transmitting 7.2 MHz broadband pulses. A single transmit focal zone was centered on the layer. Viewing the real-time, B-mode image display and adjusting the depth-gain compensation manually to give constant echo amplitude with depth over the region of interest, we recorded echo signals. Echo frames containing 312 waveforms (0.22-mm transducer pitch) of in-phase/quadrature (IQ) signals were recorded. Radio frequency (RF) signals band limited at 12 MHz were digitized at 36 Msamples/s, mixed to form IQ data, downsampled by 2.5 for electronic transfer, then

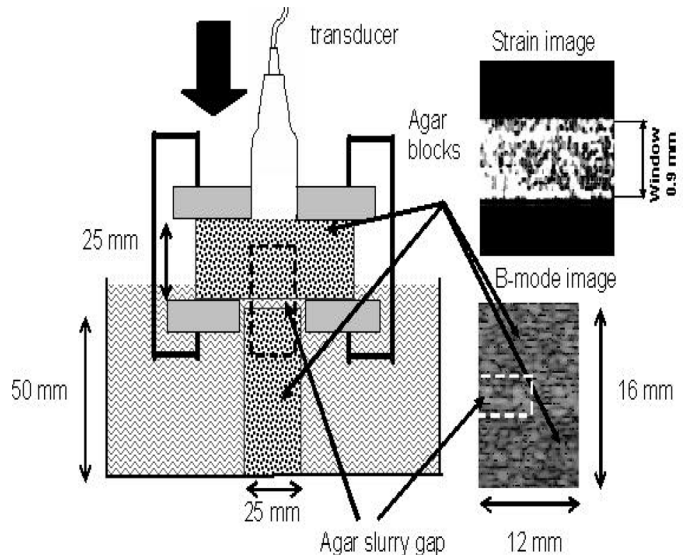


Fig. 6. The axial resolution phantom used to generate a “strain impulse” (left). B-mode image (lower right) is formed from the phantom region within the dashed box on the left. The strain image (upper right) is formed from the region in the B-mode image outlined in the white dashed lines. The thickness of the slurry-filled gap is between 0.2 and 0.4 mm.

upsampled by four before reconstituting RF waveforms. All processing was performed off-line on personal computers. The strain image in Fig. 6 shows how the correlation window determines  $LIR_\epsilon$ .

Fig. 7 shows LMTF phantom measurements processed with window lengths 1.71 mm, 0.86 mm, 0.43 mm, and 0.21 mm, respectively. Additionally, MTF curves for B-mode images (pulse only) and the correlation window are separately provided. Figs. 7(a) and (b) show that, when the correlation window length exceeds the pulse length, the axial resolution of elasticity imaging is determined by the correlation window, i.e., measurements (solid lines) track values for the correlation window (dotted lines). However, when the correlation window is smaller than the pulse length, Fig. 7(d), the LMTF curve for strain remains unchanged since spatial resolution is ultimately limited by the bandwidth of the ultrasonic imaging system; i.e., measurements (solid line) tracks values for the pulse (dotted line).

Fig. 5 summarizes measurements of  $1/u_0$  obtained from LMTF curves such as those in Fig. 7. We see that phantom measurements closely match the predicted and simulation results. The high degree of agreement is evidence that this piecewise linear model of the elasticity imaging process is able to represent experimental measurements.

## VII. DISCUSSION

There are three advantages to analyzing elasticity imaging systems from the response to a “strain impulse” [actually, a displacement ramp as in (7)]. First, the normally nonstationary correlation function can be analyzed in piecewise-WSS regions. Second, the LIR and LMTF can

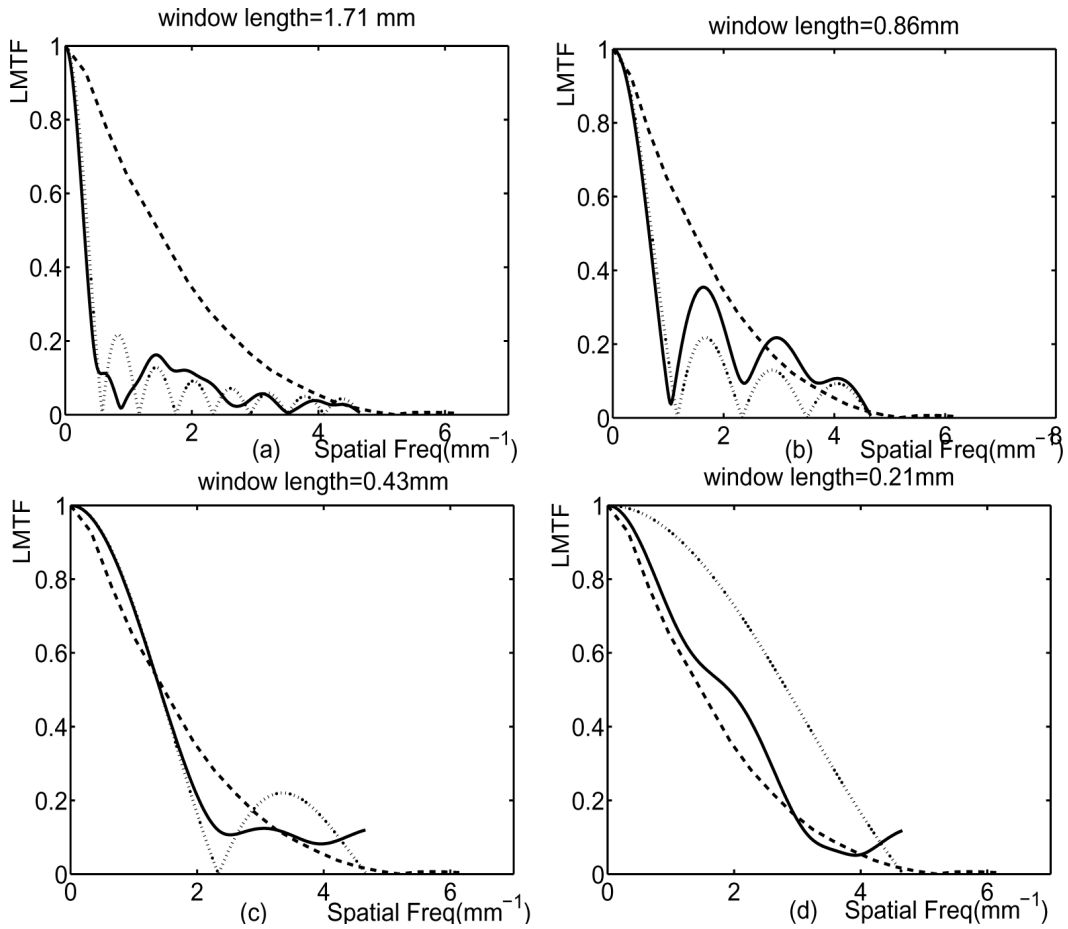


Fig. 7. Strain imaging LMTF curves for four correlation window lengths (a) 1.71 mm, (b) 0.86 mm, (c) 0.43 mm, (d) 0.21 mm. The pulse length is 0.35 mm. Dotted lines indicate LMTF curves for correlation window, and solid lines indicate measurements from phantom experiments. The dashed lines are LMTF curves for B-mode imaging.

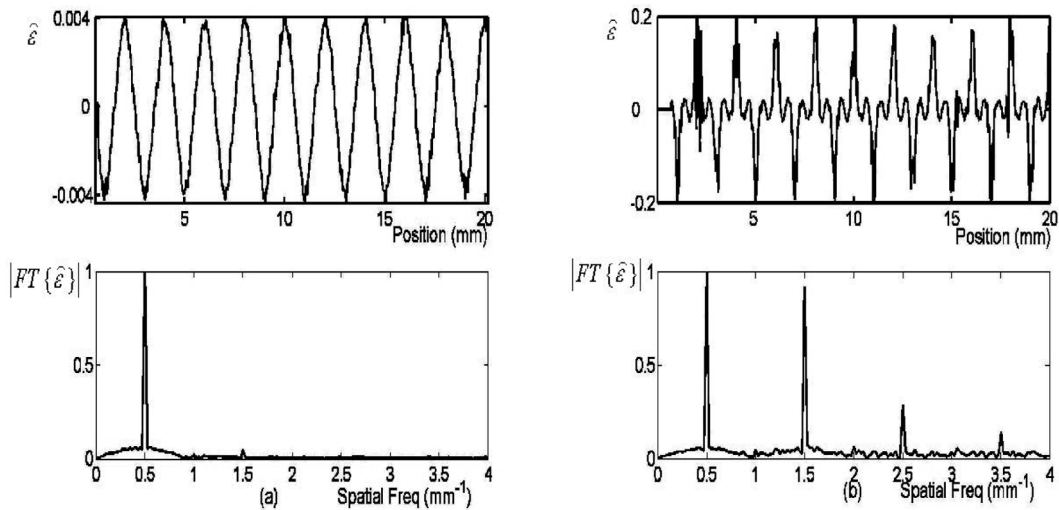


Fig. 8. Nonlinear property of strain estimators is demonstrated. (a) Estimated strain from a cosine strain input with amplitude 0.01. The frequency response is shown below. The results in (b) are the same as (a), but for an input cosine strain amplitude of 0.1.

be measured directly to define axial resolution, even if the system is shift variant. Third, the lag at the cross-correlation peak prior to interpolation is known, thus enabling derivation of an explicit expression for strain (19), despite the lack of an explicit expression for the general estimation problem (4).

The linear shift-variant form of the signal model (6), on which the entire method is based, depends on the scattering properties of the medium being independent of the applied deformation, and minimal effects of the nonlinear displacement estimator on measurements. Both assumptions are reasonable at small deformations but neither hold at larger values. The dependence of  $f(x)$  on  $\epsilon_a$  was studied previously [22]. Here we are concerned with the amount of strain that can be applied before the linear approximation breaks down.

To observe effects of the nonlinear estimator, we simulated echoes from a 1-D uniform scattering medium on which a cosine strain is applied:  $\epsilon_a(x) = A \cos(kx)$ , where the amplitude  $0.01 \leq A \leq 0.10$  and the spatial frequency was  $k/2\pi = 2$  cycles/mm. Such a deformation can be produced experimentally from the radiation force of acoustic standing waves [23]. Fig. 8(a) shows the estimated strain profile and spectrum of response for the cosine input with 1% strain amplitude. The spectrum shows there is minimal energy in the harmonics despite application of the nonlinear estimator: the ratio of third to fundamental harmonic amplitudes is 0.05. Fig. 8(b) gives the corresponding plots for 10% cosine strain amplitude. Clearly, the higher amplitude input strain has been distorted by the estimator to produce an output rich in odd harmonics. The third-to-fundamental harmonic ratio for input strains of 0.01, 0.03, 0.05, 0.07, and 0.10 are 0.05, 0.09, 0.21, 0.69, and 0.92, respectively. The distortion is much greater if the input strain has a nonzero mean, as observed previously [25], and it involves even harmonics. Harmonic generation gives the illusion of greater spatial resolution, when in fact the low frequency information is just redistributed to higher frequencies. The LIR and LMTF estimates do not apply in this situation. Figs. 3–5 and 7 clearly show that the analysis is able to accurately predict measurements up to 5% applied strain, which encompasses many imaging conditions in biological media. However, the nonlinear nature of the estimator means that the 5% applied strain limit is likely to change if we vary the input function.

Eq. (19) and (20) describe how the correlation window length, via  $N$ , the amplitude of the applied strain impulse  $\epsilon_a$ , interpolation, and properties of instrumentation, via  $h$ , determine the axial resolution of strain estimates. Provided  $\epsilon_a \leq 0.05$ , the applied strain and interpolator have negligible influence. The pulse bandwidth ultimately limits resolution, although large correlation windows used to suppress noise often determine the axial resolution in practice. Resolution in the plane normal to the sound beam axis is determined by beam properties and sampling (line density) as described by [5]. Note that this 1-D analysis and accompanying measurements ignore any effects that variations in cross-range strain will have on axial resolu-

tion. Discussions of optimal resolution inevitably rely on noise properties, which are not treated here. The approach of Fessler and Rogers [15] for nuclear imaging also seems appropriate for evaluating resolution/noise issues in elasticity imaging.

The net LMTF is not given by the product of LMTFs for the individual factors affecting axial strain resolution. Yet the data suggest that the LMTF for strain is given by the LMTF for whichever factor is most limiting, usually the correlation window.

## VIII. SUMMARY

The above results assume the correlation window shift is one sampling interval,  $cT/2$ . The window shift determines the axial strain pixel dimension. To reduce image formation time, shifts are increased from 1 to 8–16. Hence, pixel size is a factor limiting spatial resolution, e.g., see (17).

For strains larger than 5%, companding techniques (repeated correlations followed by echo warping at different spatial scales [24]) are applied to reduce the amount of strain between  $g_1$  and  $g_2$  before cross correlation. Companding is an adaptive process that varies spatially, depending on the local deformation. Although our analysis did not specifically treat companded signals—and it is possible that companding will reduce resolution—it could be examined by analyzing cascaded correlators. This report describes a linear analysis applied to elasticity imaging systems under ideal conditions.

## REFERENCES

- [1] B. Elenbaas and R. A. Weinberg, "Heterotypic signaling between epithelial tumor cells and fibroblasts in carcinoma formation," *Exp. Cell Res.*, vol. 264, pp. 169–184, 2001.
- [2] B. S. Garra, E. I. Cespedes, J. Ophir, S. R. Spratt, R. A. Zuubier, C. M. Magnant, and M. F. Pennanen, "Elastography of breast lesions: Initial clinical results," *Radiology*, vol. 202, pp. 79–86, 1997.
- [3] G. E. Trahey, J. J. Dahl, S. A. McAleavey, C. M. Gallippi, and K. R. Nighingale, "Arterial stiffness measurements with acoustic radiation force impulse imaging," *Proc. SPIE*, vol. 5035, pp. 235–241, 2003.
- [4] R. Righetti, J. Ophir, and P. Ktonas, "Axial resolution in elastography," *Ultrasound Med. Biol.*, vol. 28, pp. 101–113, 2002.
- [5] R. Righetti, S. Srinivasan, and J. Ophir, "Lateral resolution in elastography," *Ultrasound Med. Biol.*, vol. 29, pp. 695–704, 2003.
- [6] L. T. Cook, Y. Zhu, T. J. Hall, and M. F. Insana, "Bioelasticity II: Axial resolution," *Proc. SPIE*, vol. 3982, pp. 315–324, 2000.
- [7] H. C. Andrews and B. R. Hunt, *Digital Image Restoration*. Englewood Cliffs, NJ: Prentice Hall, 1977.
- [8] J. A. Fessler, "Mean and variance of implicitly defined biased estimators (such as penalized maximum likelihood): Applications to tomography," *IEEE Trans. Image Processing*, vol. 5, pp. 493–506, 1996.
- [9] F. Kallel and M. Bertrand, "Tissue elasticity reconstruction using linear perturbation method," *IEEE Trans. Med. Imag.*, vol. 15, pp. 299–313, 1996.
- [10] C. Pellot-Barakat, F. Frouin, M. F. Insana, and A. Herment, "Ultrasound elastography based on multi-scale estimations of displacement regularized fields," *IEEE Trans. Med. Imag.*, vol. 23, pp. 153–163, 2004.
- [11] F. Yeung, S. F. Levinson, and K. J. Parker, "Multilevel and motion model-based ultrasonic speckle tracking algorithms," *Ultrasound Med. Biol.*, vol. 24, pp. 427–441, 1998.
- [12] M. O'Donnell, A. R. Skovoroda, B. M. Shapo, and S. Y. Emelianov, "Internal displacement and strain imaging using ul-

trasonic speckle tracking," *IEEE Trans. Ultrason., Ferroelect., Freq. Contr.*, vol. 41, pp. 314–325, 1994.

- [13] M. F. Insana, L. T. Cook, M. Bilgen, P. Chaturvedi, and Y. Zhu, "Maximum-likelihood approach to strain imaging using ultrasound," *J. Acoust. Soc. Amer.*, vol. 107, pp. 1421–1434, 2000.
- [14] J. F. Greenleaf, M. Fatemi, and M. F. Insana, "Selected methods for imaging elastic properties of biological tissues," in *Annual Review of Biomedical Engineering*, vol. 5, M. Yarmush, Ed. Palo Alto, CA: Annual Reviews, 2003, pp. 57–78.
- [15] J. A. Fessler and W. L. Rogers, "Spatial resolution properties of penalized-likelihood image reconstruction: Spatial-invariant tomographs," *IEEE Trans. Instrum. Meas.*, vol. 9, pp. 1346–1358, 1996.
- [16] R. J. Zemp, C. K. Abbey, and M. F. Insana, "Linear system models for ultrasonic imaging: Application to signal statistics," *IEEE Trans. Ultrason., Ferroelect., Freq. Contr.*, vol. 50, pp. 642–654, 2003.
- [17] A. V. Oppenheim, R. W. Schaffer, and J. R. Buck, *Discrete-Time Signal Processing*, 2nd ed. Upper Saddle River, NJ: Prentice Hall, 1999, p. 164, 175, 300.
- [18] R. N. McDonough and A. D. Whalen, *Detection of Signals in Noise*, 2nd ed. San Diego, CA: Academic Press, 1995.
- [19] H. H. Barrett and W. Swindell, *Radiological Imaging: The Theory of Image Formation, Detection, and Processing*, vol. 1, New York: Academic, 1981, pp. 59–61.
- [20] M. M. Burlew, E. L. Madsen, J. A. Zagzebski, R. A. Banjavic, and S. W. Sum, "A new ultrasound tissue equivalent material," *Radiology*, vol. 134, pp. 517–520, 1980.
- [21] T. J. Hall, M. F. Insana, N. M. Soller, and L. A. Harrison, "Ultrasound contrast-detail analysis: A preliminary study in human observer performance," *Med. Phys.*, vol. 20, pp. 117–127, 1993.
- [22] M. F. Insana, T. J. Hall, P. Chaturvedi, and C. Kargel, "Ultrasonic properties of random media under uniaxial loading," *J. Acoust. Soc. Amer.*, vol. 110, pp. 3243–3251, 2001.
- [23] A. Hancock, M. F. Insana, and J. S. Allen, "Microparticle column geometry in acoustic standing wave beams," *J. Acoust. Soc. Amer.*, vol. 113, pp. 652–659, 2003.
- [24] P. Chaturvedi, M. F. Insana, and T. J. Hall, "2-D companding for noise reduction in strain imaging," *IEEE Trans. Ultrason., Ferroelect., Freq. Contr.*, vol. 45, pp. 179–191, 1998.
- [25] S. K. Alam and J. Ophir, "The effect of nonlinear signal transformations on bias errors in elastography," *IEEE Trans. Ultrason., Ferroelect., Freq. Contr.*, vol. 47, pp. 297–303, 2000.



**Jie Liu** received her B.S. degree and M.S. degree in Biomedical Instrument from Tianjin University, Tianjin, China, in 1995 and 1997. She obtained her Ph.D. in Biomedical Engineering from the Tsinghua University, Beijing, China, in 2001. She was a Senior Research Fellow in the Bioengineering department, University of Washington, Seattle, WA, from 2001 to 2002. She has been a Postdoctoral Researcher of Biomedical Engineering at the University of California, Davis, Davis, CA, since July, 2002.

Her research interests include developing advanced scientific theories, methods, and research techniques in medical ultrasonic imaging systems and evaluating their performances in terms of diagnostic tasks.



**Craig K. Abbey** received his bachelor's degree from the University of California, Berkeley, Berkeley, CA, in 1987, and then worked as a scientific programmer in the Department of Biochemistry and Biophysics at the University of California, San Francisco, San Francisco, CA. He obtained his Ph.D. in Applied Mathematics from the University of Arizona in 1998. He was a postdoctoral fellow at University of California, Los Angeles/Cedars-Sinai Medical Center (CSMC), Los Angeles, CA, and then a research fellow. He was a Visiting Assistant Professor of Psychology at University of California, Santa Barbara, Santa Barbara, CA, in 2001 before starting his current position as an Assistant Professor of Biomedical Engineering in July of that year.

His research interests center around evaluation of imaging methodologies in terms of diagnostic and quantitative tasks, with emphasis on the development and application of visual perception models to medical imaging.



**Michael F. Insana** (M'84) earned a B.S. in physics from Oakland University, Rochester, MI, in 1978 and the M.S. and Ph.D. degrees in medical physics from the University of Wisconsin, Madison, WI, in 1982 and 1983, respectively. He was a staff physicist at the Center for Devices and Radiological Health, U.S. Food and Drug Administration, Rockville, MD, from 1984–1987 working on ultrasonic tissue characterization, statistical analysis, and pattern recognition methods. From 1987–1999, Mike was professor of Radiology and Physiology at University of Kansas Medical Center, Kansas City, KS, where he conducted ultrasonics research involving the detection and progression of renal diseases.

His research activities include inverse scattering problems, elasticity imaging, biomaterials development, and observer performance experiments characterizing imaging systems. Since 1999, Mike has been Professor of Biomedical Engineering at the University of California, Davis, Davis, CA. He teaches courses on image science, signal processing, and system design and performance evaluation. Current research interests include wall-filters for strain-flow vascular imaging, elasticity imaging of breast tumors, coded-excitation approaches for B-mode, elasticity and Doppler estimation, and tissue-like phantoms. He is a member of the IEEE, the Acoustical Society of America, and a Fellow of the Institute of Physics.